ARTICLE

Open Access

Smart resonant micro-sensor and micro-actuator: high-performance, wide range bi-axial magnetic sensitive/ insensitive micro-device for multifunctional sensing applications

Hanin Amara [1], Nadeem Tariq Beigh [1] and Nouha Alcheikh[1✉]

Abstract

With the rapid development of intelligent and autonomous systems, such as wearable health monitoring and advanced manufacturing robots, there is a growing demand for the development of advanced, miniaturized smart sensors and actuator systems. In this context, a single microdevice with hybrid functionality as both a sensor and actuator demonstrates excellent performance across diverse applications, holds significant promise. Herein, we present a proof-of-concept for a high-performance bi-directional Lorentz force magnetometer and actuator, implemented within a single microelectromechanical system (MEMS) device. Moreover, the device demonstrates insensitivity to magnetic fields, making it highly suitable for applications that require anti-crossing behavior in magnetic environments. The design is based on a clamped-guided curved microresonator connected to straight and V-shaped beams of micro-actuators. The operation of the proposed device relies on the flexibility to control the applied electrothermal excitation in different ways, offering smart thermal actuation and dynamic sensing mechanisms. Furthermore, the proposed technique allows tuning of the first symmetric mode, achieving either a high or low frequency shift based on input power levels. Hence, this study provides valuable insights for improving tunability in sensitivity and power for various actuation mechanisms. At atmospheric pressure and an input power of 19.5 mW, the device functions as a high-performance biaxial magnetic sensor with a sensitivity (S) of ~36.58% T^{-1}, an excellent linearity in the medium-to-high magnetic field range of ±400 mT, and a minimum detectable field, B_{min} of 0.83 µT Hz^{-1}. In contrast, it can be tuned as a magnetic-field-insensitive actuator ($S = 3.28\%$ T^{-1}) with a transversal displacement of ~4 µm, utilizing a negligible power of 43 mW. The diverse operation highlights its hybrid functionality as an actuator or high-performance sensor. These features, combined with the simplicity of fabrication and low cost, make the proposed microdevice highly promising for developing a three-axis magnetic sensor and actuator network system, as well as for various industrial applications.

Introduction

The proliferation of intelligent systems, from wearable health monitoring to advanced manufacturing robots and human motion tracking, is driving an escalating demand for sophisticated, miniaturized smart sensor and actuator technologies[1,2]. The development of smart single and multi-functional sensor/actuators, hybrid micro, and nano devices is progressing, and several milestones have been reported in the literature. Most of the studies are focused on the collaboration of individual devices to achieve bi-/ multifunctional sensors and actuators. However, developing a single smart microdevice with multifunctional capabilities remains an ongoing research challenge. To meet the requirements for such systems, key performance characteristics, such as excellent sensitivity, low cost, low energy consumption, high output displacement, high integration capabilities, low cross-sensitivity and good linearity, are critical. In this context, micro-

Correspondence: Nouha Alcheikh (nouha.alcheikh@ku.ac.ae)
[1]Department of Mechanical and Nuclear Engineering, Khalifa University, Abu Dhabi 127788, United Arab Emirates

electromechanical systems (MEMS)—based sensors and actuators have emerged as suitable solutions for smart and multi-functional sensing/actuation applications[3–6].

Leveraging miniaturized mechanical and electrical components, MEMS sensors have experienced a surge in development, leading to their integration in a variety of sectors, such as automotive, consumer electronics, and healthcare, due to their enhanced performance characteristics[2]. While MEMS technology has found application in a wide range of areas, magnetic sensing has emerged as a particularly important domain, enabling the detection and measurement of magnetic fields with unprecedented precision and sensitivity. MEMS magnetic sensors have been extensively used in a wide range of emerging applications, like automotive (e.g., wheel speed sensing, electronic power steering), consumer electronics (e.g., compasses, mobile device positioning), industrial automation (e.g., current sensing, position detection), and biomedical applications (e.g., bio-magnetic field detection). Additionally, the detection of low magnetic field ranges (fT–μT Range) has become a key focus in various applications, including navigation, biomagnetism, and archaeology[7].

Currently, solid-state sensors, such as Hall effect and magnetoresistance sensors, dominate the market[8,9]. However, the detection of very low magnetic fields with sufficient precision remains a challenge for these sensors[10]. Furthermore, most commercial magnetometers are non-Lorentz-force-based and operate using principles such as the Hall effect, anisotropic magnetoresistance (AMR), giant magnetoresistance (GMR), or tunnel magnetoresistance (TMR), also known as magnetic tunnel junction (MTJ)[11]. These devices rely on magnetic materials, such as flux concentrators, which introduce several limitations. Magnetic materials can be damaged by exposure to high magnetic fields, are constrained by temperature limitations, and are prone to magnetic hysteresis. This hysteresis can reduce measurement accuracy and often necessitates frequent recalibration, adding to the operational complexity for the users[12]. Additionally, current technologies face integration challenges, particularly in developing highly sensitive sensors that can be incorporated into a single chip format, especially for Internet of Things (IoT) applications. Compatibility with CMOS processes, which is essential for creating compact systems-on-chip (SoC), remains underdeveloped[13].

Recently, Lorentz force magnetic sensors (LFMs) have emerged as a solution to mitigate such problems. Their inherent high sensitivity, wide bandwidth and magnetic material-free design complement their capability of detecting small magnetic flux densities without any undesired hysteresis effect[12,14]. Moreover, their simple and scalable design can be integrated with MEMS technology, resulting in small, lightweight, and high-

resolution devices[15]. LFMs in MEMS technology operate by utilizing the principle of the Lorentz force interactions, where a current-carrying conductor in a magnetic field experiences a force perpendicular to both the current and the field. This motion is detected through various sensing techniques, such as capacitive measurements and optical methods[15,16]. The performance and design of Lorentz force magnetometers (LFMs) are strongly influenced by their sensing mechanism and structural configuration. Capacitive LFMs rely on small capacitive gaps to achieve high sensitivity; however, these small gaps introduce viscous damping, necessitating vacuum sealing to enhance the mechanical quality factor (Q). While this approach improves performance, it adds complexity to fabrication and packaging. In contrast, thermal LFMs utilizing optical measurement techniques can function efficiently at ambient pressure, leveraging strong electromechanical coupling and an internal Q-amplification effect. These devices allow for larger capacitive gaps, simplifying fabrication while still achieving high sensitivity through the combined influence of Lorentz force interactions and thermally induced stress. LFMs have become integral to military-grade navigation systems due to their high sensitivity and multi-axis detection capabilities[16]. These sensors also find critical applications in biomedical, telecommunications, automotive, and non-destructive testing industries owing to their compact size and high resolution. Recently, MEMS-based LFMs have been reported with nT resolutions and ~1 V/T sensitivities[17–20]. However, despite remarkable performance, challenges like limited tunability and high-power consumption persist. Nonetheless, a sensor's versatility is enhanced if it can detect a magnetic field for specific applications while also being able to minimize or eliminate its interaction with the field when needed. The ability to tune the sensitivity as well as power consumption based on the application is a standout property that transforms a passive sensor into a smart and intelligent sensor system[21].

Furthermore, the integration of sensors and actuators into compact, multifunctional MEMS devices is a critical objective for next-generation intelligent systems, particularly in applications requiring dynamic reconfigurability, high sensitivity, and low power consumption. Conventional MEMS magnetic sensors and actuators are typically designed as discrete components, where magnetic sensing relies on field-sensitive materials and actuation mechanisms demand different structural or material requirements. This modularity, while beneficial for isolated performance optimization, often introduces packaging complexity, interconnect parasitics, and increased system footprint.

Therefore, in this work, we introduce a smart MEMS microdevice that demonstrates bidirectional functional tunability, operating either as a high-sensitivity Lorentz-

force-based magnetic sensor or as a magnetic-field-insensitive actuator. Our device exhibits both smart and intelligent characteristics as defined by the SAI (sensor-actuator integration) framework[22]. It is smart due to its use of multifunctional actuation and sensing through electrothermal and Lorentz mechanisms. Simultaneously, it qualifies as intelligent by enabling power-driven mode switching between actuator and sensor functionalities, demonstrating self-adaptive behavior and functional reconfiguration without structural modification or external circuitry. This places it within the emerging class of mechanically intelligent microsystems. The key enabler of smart MEMS microdevices is a power-tunable electrothermal actuation mechanism (tuning cases) that modulates the internal axial stress of a curved microbeam. This modulation, when coupled with Lorentz-force interaction under an applied magnetic field, yields a dynamic shift in the device's resonance frequency. By selectively driving different thermal actuation paths, the system smartly transitions between modes of high magnetic sensitivity and modes of stable mechanical displacement, effectively reconfiguring its behavior through internal multiphysics coupling rather than structural alteration. The resonator's intrinsic design enables intelligent and targeted activation of actuators, resulting in a broad spectrum of sensor selectivity across various input power levels. In our proposed design, we have meticulously considered and addressed potential process compatibility issues between magnetic sensing (based on Lorentz force and mechanical resonance) and electrothermal actuation. This work overcomes the pertinent issues in multi-chip heterogeneous integration by utilizing a single-chip, multifunctional design. Our design features a single-chip clamped-guided curved microbeam linked to a straight micro-actuator and two V-shaped microactuators, facilitating the application of a biaxial thermal axial load-Lorentz force interaction for better magnetic field sensing.

The proposed sensor' tunability and magnetic sensitivity are analyzed through simulations and experiments. Section "Device description" covers device design and operation, Section "Materials and methods" details fabrication, experimental, and simulation setups, and Section "Results and discussions" presents modeling, results, and performance evaluation. Section "Conclusion" concludes with key findings and future research directions.

Device architecture and functional mechanism

Figure 1a shows the perspective-view schematic of the proposed in-plane microresonator. The microresonator is fabricated using the SOIMUMPs® process flow from MEMSCAP. The structural features of the MEMS resonator device incorporate a clamp-guided curved microbeam along with the tunable actuating structure and fixed electrodes. On the left, the structure consists of V-shaped beams (V_1 and V_2) and a double-clamped straight beam (SB) arranged in two sets. On the right, the clamp-guided curved microbeam is shown alongside the fixed electrodes positioned on either side of the microbeam, enabling actuation through a capacitive coupling mechanism. The as-fabricated optical image of the microresonator (Fig. S1) and geometrical dimensions of all the components are detailed in Table S1 of the Supplementary Information. The actuator beam pairs are designed to generate bi-axial stress along the length of the microbeam by the application of different combinations of DC voltages across them. The device consists of actuation electrodes A–G that can be specifically driven at a given V_{DC} or connected to the ground (GND). Therefore, multiple combinations of actuation or tuning cases can generate axial stress in the microbeam and result in different thermal currents (I_{Th}) across the actuator beams. Further, electrode H electrostatically drives the curved microbeam into resonance via an AC–DC voltage ($V_{AC} + V_{DC} = 35$ V).

Principle of operation: microbeam axial stress tuning

The device works on the principle of "resonance frequency shift" in the curved microbeam by introducing intentional bi-axial loading in it. The bi-axial loading is introduced via a smart tuning mechanism by various combinations of actuation electrodes. The capability of bi-axial loading results in compressive or tensile axial forces in the curved microbeam (Fig. 1b). This causes bi-directional stiffness modulation and thereby can offer diverse device dynamics that evolve into considerable sensitivity gains (Fig. 1c). In this work, we will discuss 6 tuning cases. The tuning cases and their actuation parameters are tabulated in Table 1. A terminal marked with V is given a DC voltage V_{Th}, or else is grounded if it is designated as GND. Any actuation case, when activated, causes two important phenomena. Firstly, it produces an axial load on the guided end of the microbeam. The axial stress is attributed to the electrothermally induced stress due to Joule's heating mechanism originating from the thermal current I_{Th}. This phenomenon induces thermal expansion in the actuator beams, generating a displacement of the shuttle along the positive x-axis and imposing a compressive axial load on the microbeam. These compressive forces alter the microbeam's stiffness, consequently modifying its resonance frequencies. The second phenomenon is discussed in the next section.

Principle of operation: Lorentz-force magnetometer

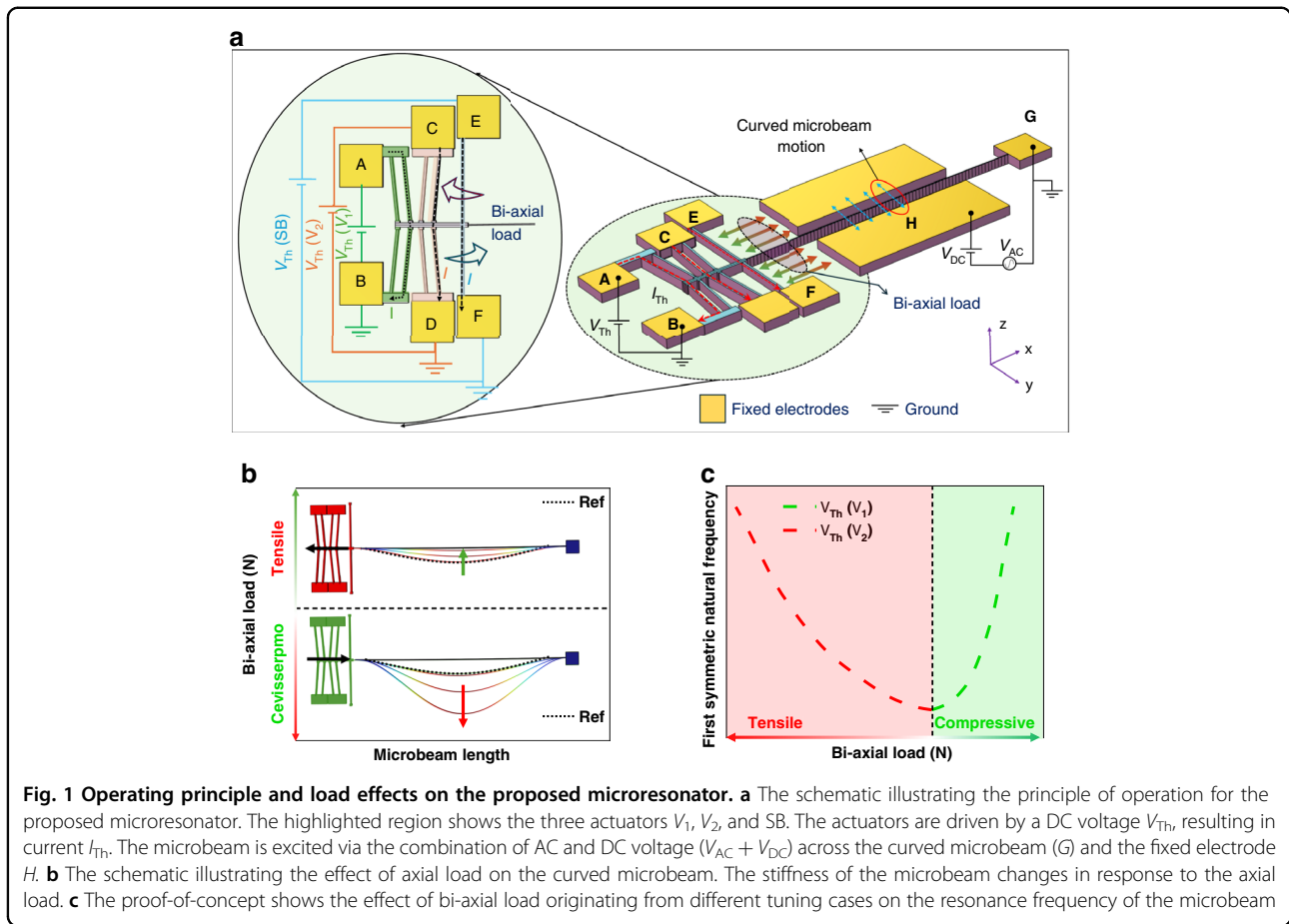Figure 2a illustrates the proposed in-plane microresonator as a magnetometer. The induced thermal

Fig. 1 Operating principle and load effects on the proposed microresonator. a The schematic illustrating the principle of operation for the proposed microresonator. The highlighted region shows the three actuators V_1, V_2, and SB. The actuators are driven by a DC voltage V_{Th}, resulting in current I_{Th}. The microbeam is excited via the combination of AC and DC voltage ($V_{AC} + V_{DC}$) across the curved microbeam (G) and the fixed electrode H. **b** The schematic illustrating the effect of axial load on the curved microbeam. The stiffness of the microbeam changes in response to the axial load. **c** The proof-of-concept shows the effect of bi-axial load originating from different tuning cases on the resonance frequency of the microbeam

Table 1 Tuning cases for the microresonator

Case	Tuning parameters
Case V_1	A = V; B = GND
Case V_2	C = V; D = GND
Case SB	E = V; F = GND
Case V_1_V	A & G = V; B = GND
Case V_2_V	C & G = V; D = GND
Case SB_V	E & G = V; F = GND

current, I_{Th}, interacts with the external out-of-plane magnetic field, B_z, resulting in a multi-physical coupling between structural dynamics, electric current, and the magnetic field. This interaction gives rise to the Lorentz force ($F_L = l(I_{Th} \times B_z)$), which acts synergistically with the thermally induced axial stress. This coupling mechanism facilitates precise modulation of the resonance frequency shifts in response to the applied magnetic field, enabling effective magnetic sensing. The DC out-of-plane bi-directional magnetic flux, B_z, is generated by permanent

magnets strategically positioned beneath the device. Based on the direction of B_z, a positive or negative Lorentz force interaction results in a considerable shift in resonance frequency of the curved microbeam, as shown in Fig. 2b.

Materials and methods
Fabrication process

The microresonator is fabricated using the cost-effective SOIMUMPS® process, starting with an SOI wafer and involving PSG doping, DRIE etching, and vapor HF oxide removal (more can be found in the Supplementary Material Fig. S2 for a detailed explanation)[20].

Experimental setup

The experimental setup for characterizing the in-plane MEMS resonator uses a Polytec VibroFlex Laser Doppler Vibrometer system (illustrated in Fig. S3 of the Supplementary information). The system integrates various modules and connections to measure and analyze the behavior of the MEMS device. The device was excited at its first in-plane resonant mode (symmetric), occurring at 33.3 kHz, via the H–G electrodes. The thermal voltage (V_{Th}) is varied between 0 and 6 V, generating a thermal
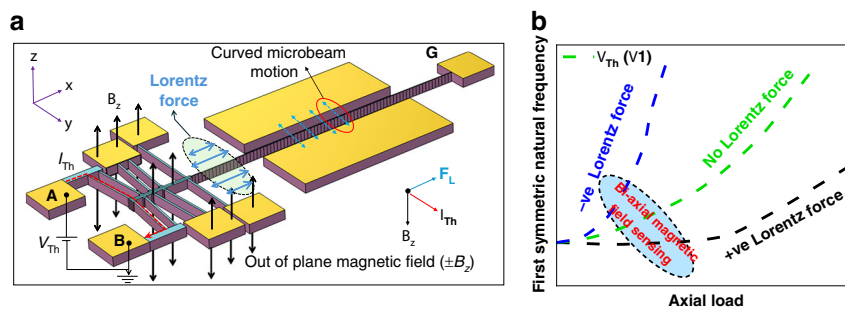
Fig. 2 Principle and demonstration of Lorentz-force-based tuning in a microresonator. a The schematic illustrating the principle of operation for the proposed microresonator. The schematic highlights electrical connections corresponding to different tuning cases, the direction of the applied magnetic field and the direction of generated Lorentz forces. **b** The proof-of-concept shows the effect of the bi-axial Lorentz force on the first symmetric resonance frequency on the microbeam. The direction of the generated Lorentz force facilitates the tensile or compressive axial forces on the curved microbeam and hence modulates the first symmetric in-plane resonant mode (f_1)

current (I_{Th}) ranging from 0 to 23 mA across the actuators V_1, V_2, SB, and the curved microbeam, respectively. Notably, the actuator beams vis-à-vis the actuation cases exhibit distinct electrical and mechanical resistances, attributed to their specific geometric/structural designs and electrical paths. Therefore, the sensor performance changes significantly between various tuning cases.
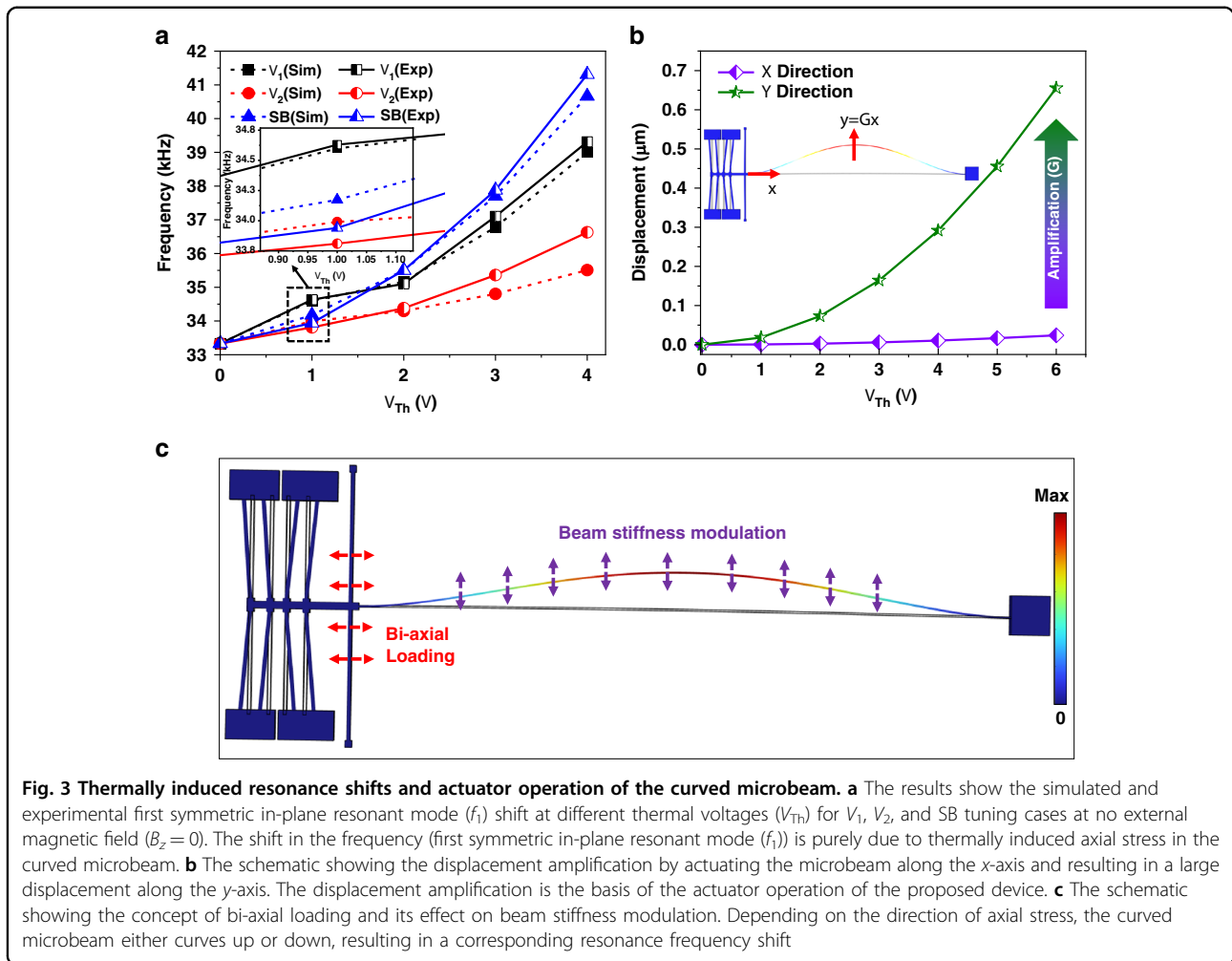
Simulation model configuration

Our finite element model (FEM) was developed in COMSOL Multiphysics 6.2 (simulation workflow is illustrated in Fig. S4). We utilized the coupled multiphysics simulations by integrating the scientific principles across the domains of heat transfer, solid mechanics, and electrical currents. We used thermal expansion multiphysics coupling to connect the thermal and mechanical domains, which ensured that temperature changes from Joule heating were directly translated into mechanical deformations. To perform eigenfrequency analysis, we first define the material properties, apply our boundary conditions such as fixed constraints, and select an appropriate mesh to capture mode shapes accurately. The study then solves the lowest eigenfrequencies, revealing the fundamental vibration modes of the MEMS structure. To compute the mid-point displacement of the MEMS curved beam under different applied thermal voltages V_{Th}, we used the solid mechanics module in COMSOL, integrating it with the heat transfer and electrical current physics. A stationary study was performed to determine the static mid-point displacement response of the curved beam at varying V_{Th} values, highlighting how thermal load impacts mechanical deformation.

Results and discussions
Finite element method and experimental validation

To evaluate the effect of V_{Th} on the dynamic and static response of the curved microbeam, we simulated the first symmetric in-plane eigenfrequency (Illustrated in Fig. S5)

and mid-point displacement as a function of V_{Th}. To determine the displacement values for each of our cases, first we validated our finite element model (FEM) by simulating the eigen frequencies and comparing them to the experimental values. The graph shown in Fig. 3a compares the simulation results from the COMSOL finite element model (FEM) with experimental data for the frequency response of different modes (V_1, V_2, and SB) of a MEMS resonator as a function of thermal voltage (V_{Th}). Each mode is presented with simulation results (dotted lines) and corresponding experimental data (solid markers), enabling direct comparison. For all modes (V_1, V_2, and SB), the COMSOL simulation and experimental data show consistent trends. Both the simulated and measured frequencies increase nonlinearly with V_{Th}, indicating that the FEM model accurately captures the physical behavior of the MEMS resonator under thermal loading, which arises due to electrothermal and electromechanical coupling in the resonator. The frequency values predicted by the FEM model closely align with the experimental data across the entire voltage range. The differences between simulation and experiment are minimal, with deviations within an acceptable range for modeling accuracy. The calculated coefficients of determination for $V1$, $V2$, and SB, respectively, are 0.992, 0.988, and 0.999. This demonstrates the validity of the model's setup assumptions and parameters. For V_1, the FEM model closely matches experimental values, particularly at higher voltages, where nonlinear effects become more pronounced. For V_2, the simulation aligns well with the experimental data, although slight deviations occur at intermediate voltages, possibly due to fabrication tolerances or unmodeled secondary effects. For SB, the agreement between simulation and experiment is excellent, with almost identical trends and values. This demonstrates that the COMSOL FEM model provides a reliable representation of the MEMS resonator's frequency response under

Fig. 3 Thermally induced resonance shifts and actuator operation of the curved microbeam. a The results show the simulated and experimental first symmetric in-plane resonant mode (f_1) shift at different thermal voltages (V_{Th}) for V_1, V_2, and SB tuning cases at no external magnetic field ($B_z = 0$). The shift in the frequency (first symmetric in-plane resonant mode (f_1)) is purely due to thermally induced axial stress in the curved microbeam. **b** The schematic showing the displacement amplification by actuating the microbeam along the x-axis and resulting in a large displacement along the y-axis. The displacement amplification is the basis of the actuator operation of the proposed device. **c** The schematic showing the concept of bi-axial loading and its effect on beam stiffness modulation. Depending on the direction of axial stress, the curved microbeam either curves up or down, resulting in a corresponding resonance frequency shift

thermal voltage. Thermomechanical systems harness the Joule heating effect to convert thermal energy into mechanical displacement.

Figure 3b highlights the interplay between thermal and mechanical loads. As shown, the thermal load applied along the x-axis leads to an amplified displacement along the y-axis. The amplified displacement in the y-axis is due to the involvement of the mechanical structures (V-shaped structure, straight beam) that translate the small thermal loads into large mechanical displacements through leverage mechanisms. This mechanical displacement is bi-directional as the V-shaped structures allow a bi-axial load in the positive and negative x-axis directions when they thermally expand (Fig. 3c). The applied biaxial load induces changes in the beam's curvature, and this modulation directly impacts the mechanical behavior of the structure, including its stiffness and frequency response.
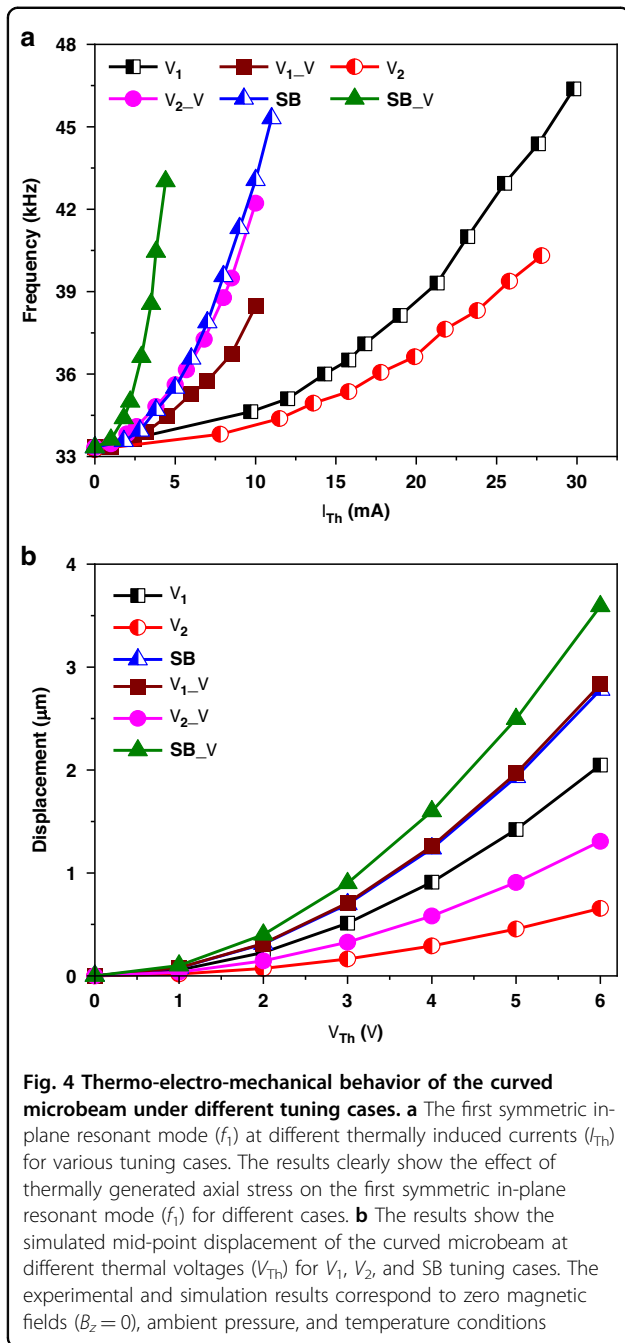
Multifunctional hybrid microdevice analysis

In order to develop a versatile MEMS device that can be tuned for certain use cases by balancing sensitivity, power

efficiency, and operational range, it is essential to be able to obtain varied frequency responses across multiple configurations. This makes the microdevice suitable for a variety of applications, such as signal processing, actuation, and sensing. In order to investigate the possible applications of each configuration, we examined the static and dynamic responses for various tuning scenarios.

Thermal-electromechanical tuning

The graph shown in Fig. 4a illustrates the relationship between the thermal current (I_{Th}) and the first in-plane symmetric mode frequency in the absence of an external magnetic field (B_z) for the different tuning cases of the MEMS resonator (additional cases are provided in Table S2 and Fig. S6). In all cases, the resonance frequency increases nonlinearly with I_{Th}, demonstrating thermal tuning. This occurs because current-generated heat alters the resonator's mechanical properties, specifically its stiffness. Applying voltage to the curved beam amplifies this thermal tuning, resulting in a greater frequency shift. This enhancement stems from two effects: electrothermal

Fig. 4 Thermo-electro-mechanical behavior of the curved microbeam under different tuning cases. a The first symmetric in-plane resonant mode (f_1) at different thermally induced currents (I_{Th}) for various tuning cases. The results clearly show the effect of thermally generated axial stress on the first symmetric in-plane resonant mode (f_1) for different cases. **b** The results show the simulated mid-point displacement of the curved microbeam at different thermal voltages (V_{Th}) for V_1, V_2, and SB tuning cases. The experimental and simulation results correspond to zero magnetic fields ($B_z = 0$), ambient pressure, and temperature conditions
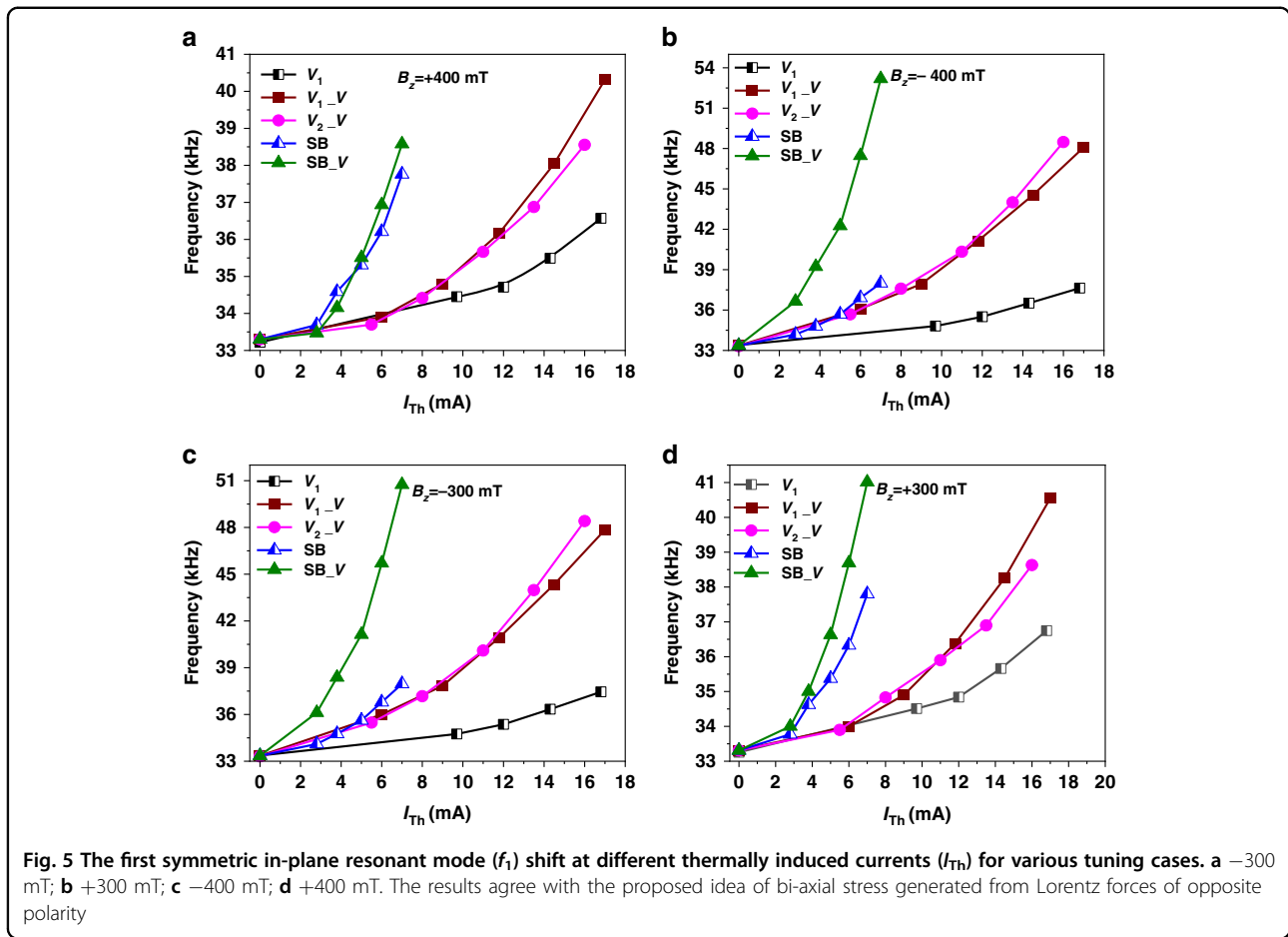
inputs, resulting in a more pronounced frequency shift. The applied voltage additionally augments thermal tuning. Furthermore, a nonlinear increase in frequency with I_{Th} is characteristic of thermal effects in MEMS devices, where elevated currents induce greater thermal expansion or stress variations. This is evident from the consistent upward shift in the frequency of all voltage-applied (to the end of the curved beam) modes (V_1_V, V_2_V, and SB_V) compared to their non-voltage counterparts (V_1, V_2, and SB).

Static analysis of actuator operation

Displacement is a key factor in MEMS performance, with larger displacements enhancing sensitivity in sensing applications or improving actuation efficiency. The displacement for all tuning cases increases nonlinearly with V_{Th}, reflecting the cumulative effects of thermal loading and electromechanical interactions (Fig. 4b). The SB_V tuning case exhibits the most significant displacement, with a sharp increase beyond $V_{Th} = 4$ V, reaching 3.60 μm at $V_{Th} = 6$ V. This indicates that SB_V is more sensitive to V_{Th} as compared to the other cases. The other tuning cases, SB, V_1, V_2_V, and V_2 result in the maximum displacement of 2.83, 2.77, 2.05, 1.31, and 0.65 μm, respectively. The low displacement observed in mode V_1_V is likely due to its structural configuration, resulting in a reduced response to thermal loading compared to case SB_V. The intermediate displacement in V_1 case shows a balanced response, overcoming the structural rigidity, making this mode suitable for applications requiring controlled motion without excessive deformation. The V_2_V case exhibits a more gradual increase and hence can provide greater stability with lower sensitivity to external inputs, which could be useful for applications requiring precision. Finally, the V_2 case, representing the lowest displacement mode, indicates a stiffer configuration with lower thermal expansion, ideal for precise, stable operations rather than large actuation.

While the microdevice exhibits functional duality, enabling both sensing and dynamic reconfiguration through electrothermal actuation, it is evident that the integrated actuator does not directly interact with the external environment (applying a mechanical force, displacement, or torque to an external object or medium (e.g., fluid, optical element, and biological tissue)).

However, we note that the device generates significant in-plane displacement ($\sim$3.6–4 μm) under low-voltage thermal excitation, which, if mechanically coupled to a compliant external interface, could feasibly be harnessed for contact switching or triggering applications. This is particularly relevant for systems that require microscale actuation with reconfigurable states, such as MEMS logic elements or mechanical relays. Nevertheless, due to the presence of the excitation electrode, the microbeam can

stiffening, where a DC voltage applied to the actuators creates a thermally induced axial force and increased electromechanical coupling. This axial force adds an extra term to the resonator's equation of motion[23], which influences the resonance frequency.

Electromechanical coupling is observed as an enhancement in the interaction between the beam's mechanical motion and the excitation electric field due to an applied DC voltage. This amplified coupling increases the system's responsiveness to both thermal and electrical

Fig. 5 The first symmetric in-plane resonant mode (f_1) shift at different thermally induced currents (I_{Th}) for various tuning cases. a −300 mT; **b** +300 mT; **c** −400 mT; **d** +400 mT. The results agree with the proposed idea of bi-axial stress generated from Lorentz forces of opposite polarity

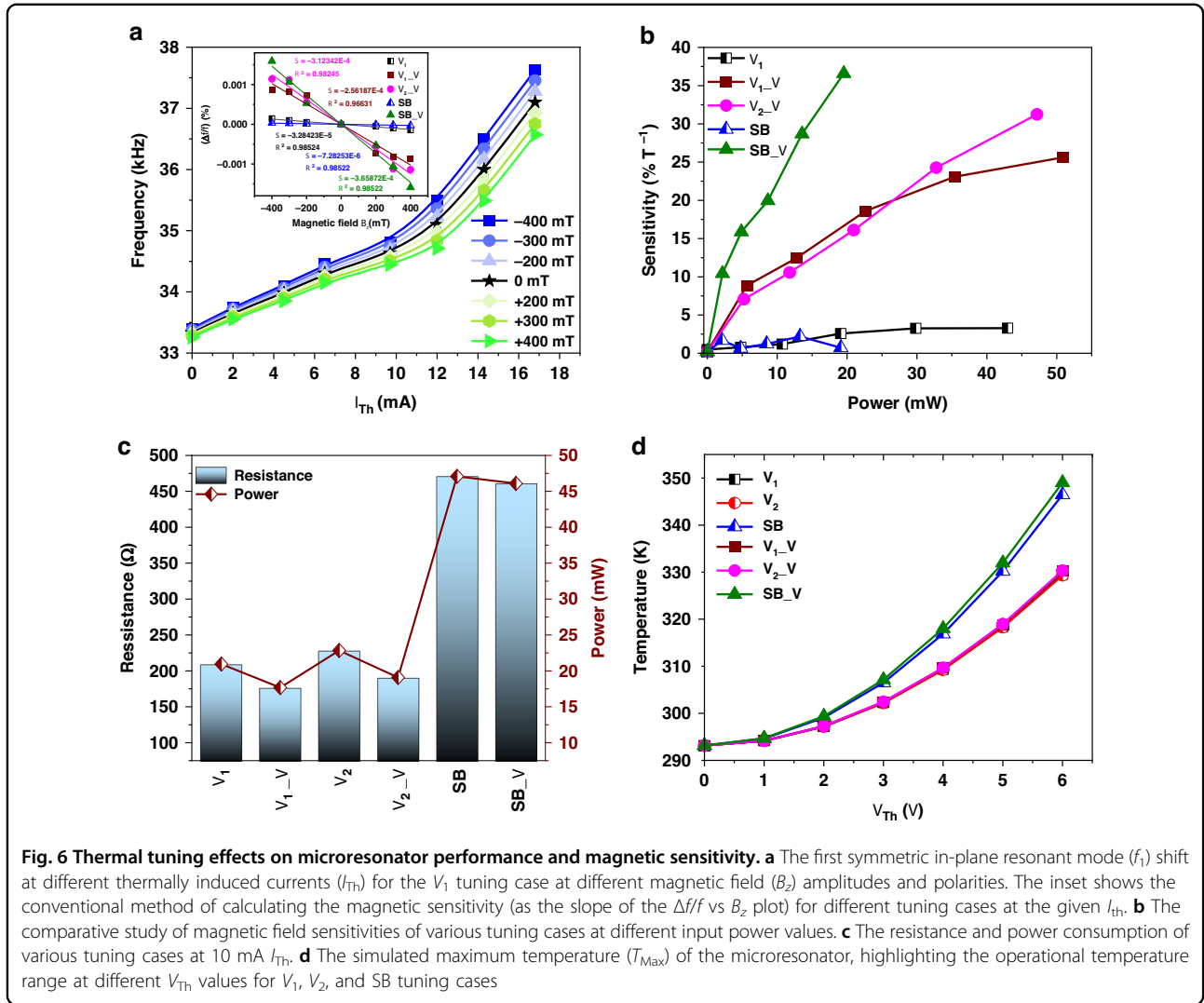be used as a capacitive switch, a flow controller in microfluidic channels, etc.

Displacement analysis is crucial for optimizing MEMS actuator performance, ensuring efficient and reliable motion control with minimal energy use.

Dynamic analysis of magnetic field sensing

We studied the dynamic response for different tuning cases to explore the potential use of each configuration. The experimental data in Fig. 5 reveal distinct differences between the structural modes of the MEMS resonator based on their frequency responses to thermal voltage (V_{Th}) and the applied magnetic field (±200, ±300, ±400) (more data on other cases can be found in Fig. S7). General observations indicate that all modes show nonlinear responses to V_{Th}, with frequency and displacement increasing due to thermal-induced stress and expansion. The nonlinear trends across all graphs reflect the complex interplay of thermal expansion, axial forces, Lorentz force (F_L), and electromechanical coupling in the MEMS resonator.

The SB_V mode consistently demonstrates the highest sensitivity to the magnetic field, making it the most responsive tuning case of the system. It exhibits the steepest frequency shift with increasing V_{Th}, reflecting its high thermal sensitivity due to lower initial stiffness and a more pronounced axial force and Lorentz force effect. It reaches the highest frequencies compared to all the other cases. Additionally, the frequency shift of all cases increases with the magnetic field directed to the negative z-axis, creating a Lorentz force that enhances the axial force, bending the curved beam further. However, the magnetic field positioned in the positive z-axis creates a Lorentz force that opposes the axial force direction, creating a lower bend in the curved beam. The V_1_V and V_2_V modes show a moderate frequency increase comparable to the SB mode frequency shift, but notable enhancements to the V_1 and V_2 cases. The V_2 mode demonstrates the smallest frequency shift among the three modes, indicating higher stiffness or less thermal coupling compared to the other cases. Furthermore, it could also be due to the V-shaped beam being slanted opposite the axial force's direction. This makes V_2 best suited for applications where stability and lower sensitivity to the magnetic effects in this range are preferred.

Fig. 6 Thermal tuning effects on microresonator performance and magnetic sensitivity. a The first symmetric in-plane resonant mode (f_1) shift at different thermally induced currents (I_{Th}) for the V_1 tuning case at different magnetic field (B_z) amplitudes and polarities. The inset shows the conventional method of calculating the magnetic sensitivity (as the slope of the $\Delta f/f$ vs B_z plot) for different tuning cases at the given I_{th}. **b** The comparative study of magnetic field sensitivities of various tuning cases at different input power values. **c** The resistance and power consumption of various tuning cases at 10 mA I_{Th}. **d** The simulated maximum temperature (T_{Max}) of the microresonator, highlighting the operational temperature range at different V_{Th} values for V_1, V_2, and SB tuning cases

Performance metrics of a hybrid microdevice

A thorough understanding of key performance metrics such as sensitivity, power consumption, operational temperature, operational speed, and minimum detectability is essential for selecting the most suitable sensor for a given application and optimizing system design. Moreover, performance evaluation methodologies enable the identification of potential limitations and sources of error, facilitating the development of improved sensor designs and calibration techniques.

Sensitivity

The sensitivity of a MEMS magnetometer quantifies its ability to detect minute changes in magnetic fields. Herein, the sensitivity is calculated by applying an out-of-plane bi-directional magnetic field B_z using permanent magnets and computing the shift in the first-symmetric in-plane resonance mode (f_1). The experiments are performed for magnetic field intensities ranging from −400 mT to +400 mT.

The interaction of bias current (I_{Th}) and B_z generates a proportionate Lorentz force (F_L), which acts in synchronization with the thermally induced axial, modulating the stiffness of the curved microbeam. The stiffness modulation results in significant frequency shifts and hence a notable magnetic sensitivity is achieved. In this context, it can be stated that the higher bias currents can improve the sensitivity of a magnetometer. As an example, Fig. 6a shows the frequency tunability for case V_1 at different magnitudes and polarities of B_z. The magnetic field introduces a Lorentz force that interacts with the microbeam resonator, causing frequency shifts, with positive magnetic fields (+200, +300, +400 mT) decreasing the resonant frequency compared to the baseline (0 mT), and negative magnetic fields (−200, −300, −400 mT) increasing the resonant frequency relative to the baseline. The frequency shifts are symmetrical around 0 mT, reflecting the bi-directional sensing capability of the proposed magnetometer. It can be observed that at higher bias currents ($I_{Th} > 12$ mA), the frequency shifts

become more pronounced due to increased thermally induced axial load and Lorentz force. This phenomenon is true in all the tuning cases.

The inset in Fig. 6a highlights the sensitivity calculations for different tuning cases at a given V_{Th}. The sensitivity (S) is calculated as the slope of % relative shift in resonance frequency ($\%\Delta f/f$) and applied magnetic field B_z. It is previously reported that the magnetic sensing capability of the microresonator improves significantly with power due to increased signal strength, resulting in elevated thermal effects and the introduction of nonlinear dynamics. Furthermore, higher power allows stronger mechanical and electrical responses to the magnetic field, improving the signal-to-noise ratio (SNR). Therefore, power-induced Joule heating can alter the sensor performance and amplify its response to the Lorentz force. Figure 6b illustrates the sensitivity of each tuning case at different input power levels (Please refer to Fig. S8 for sensitivity calculations). The input power level is determined by the bias voltage (V_{Th}) and the inherent resistance offered by each case. It is observed that the magnetometer can project a diverse range of sensitivities over different power ranges. Particularly, case SB_V shows the steepest sensitivity growth within a narrow power range, reaching a maximum sensitivity of ~36.59% T^{-1} at ~19.5 mW. On the contrary, tuning case V_1 exhibits a slow and nearly linear increase in sensitivity with power, reaching ~3.2% T^{-1} at ~43 mW Hence, the insensitivity to the magnetic field in the case of V_1 demonstrates the potential of the proposed device for other sensing applications, such as gas sensing[24].

The tuning cases SB_V and V_1 represent the two extremes of the proposed microdevice, offering high sensitivity in a small power range and vice versa. It is important to note the correlation between displacement-voltage characteristics and the sensitivity–power trends (particularly for the SB_V configuration). The SB_V mode demonstrates the steepest increase in magnetic sensitivity with respect to power input while also exhibiting the largest displacement at the lowest power consumption range. The other tuning cases offer performance in-between SB_V and V_1, respectively. A high-sensitivity, narrow-power-range configuration is beneficial for detecting weak magnetic fields, such as in biomedical imaging or space magnetometry. Conversely, a low-sensitivity, large-power-range setup is advantageous for applications requiring a linear response. Systems monitoring magnetic field variations in equipment may benefit from steady, moderate sensitivity to avoid cross-sensitivity to noise.

Wearable sensors or remote sensing systems prioritize steady sensitivity to extend operational lifetimes without sacrificing reliability. High sensitivity (e.g., (SB_V)) enhances detection but may introduce challenges like overheating, material fatigue, or instability at high power levels. Steady sensitivity configurations (e.g., (V_1)) offer greater robustness and simplicity, making them suitable for environments where precision is less critical than durability and efficiency. These findings highlight the trade-offs involved in designing Lorentz force MEMS sensors. Configurations like (SB_V) demonstrate exponential sensitivity growth with power, which is ideal for detecting weak magnetic fields. In contrast, configurations like (V_1) provide stable, predictable sensitivity growth, favoring low-power, reliable applications. The ability to tailor sensitivity by adjusting power and configuration makes these sensors versatile for diverse fields, from precision biomedical imaging to industrial automation.

Power consumption

The different tuning cases offer a different set of resistances, attributed to the different combinations of actuator-beam pairs[25]. For simplicity, each tuning case is compared at a fixed thermal current $I_{Th} = 10$ mA. Power increases linearly with resistance for fixed current, following the relationship ($P = I^2R$). As observed in Fig. 6c, the configurations (V_1) through (SB_V) have varying resistances, with (SB) and (SB_V) showing the highest resistances (approximately 450 Ω), and (V_1), (V_1_V), (V_2), and (V_2_V) showing lower and more uniform resistances, around 200–250 Ω. Power consumption follows a similar trend to resistance, being relatively low (around 15–25 mW) for configurations V_1, V_1_V, V_2, and V_2_V, and spiking to approximately 45–50 mW for configurations SB and SB_V. High-resistance configurations (SB, SB_V) consume more power due to their higher resistance, leading to increased Joule heating, which in turn amplifies the sensitivity. This aligns with the high-sensitivity values found in Fig. 6b. These configurations are better suited for high-sensitivity applications where power efficiency is less critical. Low-resistance configurations consume less power and exhibit lower heat generation, making them ideal for low-power applications or scenarios where long-term operation is needed, such as portable or battery-powered sensors. However, their lower power and resistance reduce their sensitivity to magnetic fields. This highlights the trade-offs between resistance and power consumption across different configurations. High resistance configurations consume more power, enhancing performance at the cost of efficiency and thermal management challenges, and lower resistance configurations favor power efficiency and robustness but potentially sacrifice sensitivity. The configuration choice depends on the specific application requirements, balancing sensitivity, power consumption, and thermal stability.

Operational temperature

The relationship between the device temperature (T) and the power curve is rooted in Joule heating, primarily driven by the bias voltage as electrical power dissipates as heat in the MEMS device during static and dynamic operation (Animation of temperature distribution effect can be found in Fig. S9). As shown in Fig. 6d, the (SB_V) configuration shows the steepest increase in temperature, aligning with its higher resistance and power dissipation seen in the earlier graph. (SB_V)'s high sensitivity is partially due to thermal effects amplifying the Lorentz force and material deformation. (V_1, V_2, V_1 _V and V_2_V) show a more gradual increase in temperature, consistent with their lower resistance and power dissipation, designed for more power-efficient, stable operation with less Joule heating. All tuning configurations operate well below the melting temperature of silicon (~1687 K), ensuring safe and reliable performance for both sensing and actuation. The power curve from the resistance-power graph (Fig. 5c) shows that (SB, SB_V) consumes the most power at higher resistance, directly correlating with the sharp temperature rise in this graph. Conversely, (V_1, V_2, V_1 _V and V_2_V) consume less power, leading to lower temperatures for the same voltage. Increased temperature due to Joule heating can enhance sensor sensitivity, as seen in the earlier sensitivity-power graph (Fig. 5b), benefiting the (SB_V) configuration and making it ideal for high-sensitivity applications. Lower power configurations like (V_1, V_2, V_1 _V and V_2_V) prioritize stability and efficiency over sensitivity, demonstrating the trade-offs between sensitivity, power consumption, and temperature management in MEMS sensor design.

Minimum detectable field

The detection method of a magnetic sensor, based on Joule's heating and electrostatic actuation, faces several challenges due to parasitic effects and various sources of noise, which can significantly influence the resolution of the measurements. Additionally, thermo-mechanical noise, such as Brownian motion, is a critical factor in MEMS devices, particularly when operating at ambient pressure, as it depends on parameters like temperature, damping coefficient, and quality factor (Q). The measured quality factor (Q) of the sensor was found to be 60[26], and the damping coefficient was calculated to be $b = 0.0083$ (please refer to Table S3 for detailed information on parameters used for B_{min} calculations). The Brownian noise equivalent magnetic field detection limit is given by Eq. (1):

$$B_{min} = \frac{F_B}{L I_{Th}} = \frac{\sqrt{4 k_B Tb}}{L I_{Th}} \tag{1}$$

Where in F_B is the Brownian noise of the resonator, k_B is the Boltzmann constant, T is the operating temperature, b is

the damping coefficient, L is the electrical path length of the tuning case, and I_{Th} is the thermally induced current. B_{min} is found for the least for tuning case SB_V and is calculated to be $0.83\,\mu T\,Hz^{-1}$. Table S4 highlights the B_{min} values for all tuning cases. The value is calculated at 10 mA current. An in-vacuum operation can do further enhancement in B_{min} to improve the Q-factor (B_{min} ω $\sqrt{b}$) and reduce the damping coefficient, or by increasing the microbeam length or input current. However, both the latter parameters are limited by the geometrical considerations and power consumption limits.

Operational speed

The operational speed of the microresonator is a critical performance metric and is defined as the rate of change of resonance frequency of the microbeam upon the application of electrothermal voltage. The characteristic time associated with the heating and cooling of the microbeam is much longer than the period its resonance vibrations. The operational speed is therefore limited by the electrothermal time constant (t_{et}) of the microbeam and is calculated as in Eq. (2)[27]:

$$t_{et} = \left[\frac{\pi^2 K_{si}}{c \rho l^2} + \frac{C_f K_{air}}{g h c \rho} \right]^{-1} \tag{2}$$

Based on Eq. (2), the electrothermal time constant t_{et} for the microbeam at room temperature is calculated to be 551 μs, which indicates a maximum achievable electrothermal speed of 1.8 kHz.

Linearity

Linearity is crucial for accurate and reliable sensor performance, enabling precise data acquisition and minimizing errors in signal processing. The linearity is calculated using the least squares method for each tuning case. The coefficient of determination (R^2) quantifies how well the linear fit represents the data. The R^2 values (e.g., 0.99692) indicate strong linear correlations, demonstrating that tuning thermal bias current can optimize sensitivity while maintaining linearity in magnetic field detection. The %linearity is given by (R^2*100)%. For the proposed magnetometer, we compare the %linearity of each tuning case at $V_{Th} = 3\,V$. The % linearity for V_1, V_1_V, V_2_V, SB, and SB_V is 98.5%, 96.6%, 98.2%, 98.5%, and 99.6%, respectively. The high linearity for each tuning case establishes that the proposed sensor has a highly reliable and smart magnetometer. The sensitivity calculations for other V_{Th} values are detailed in the Supplementary Information.

As evidenced in Table 2, the proposed device surpasses our previous design[28], by offering a high sensitivity, bidirectional, magnetic field sensing while maintaining excellent linearity. While exhibiting lower sensitivity, the

Table 2 **Table of comparison with the state-of-the-art MEMS magnetic sensors**

MEMS MS	Power (mW)	Sensitivity (T^{-1})	Range (mT)	Linearity	Sensing method
[29]	300×10^{-3}	0.0325	±13	0.985	Electromechanical frequency readout-closed loop (vacuum)
[14]	125×10^{-3}	4.739e-3	Up to 3.6	0.99	Electromechanical frequency readout-closed loop (air)
[30]	–	–	Up to 3.66e-3	–	Optical (vacuum)
[31]	–	1.636e-4	0–500	–	Piezoresistive-open loop (air)
Previous work[28]	0.2	2.56	8–400	0.9988	Optical-open loop (air)
This work	19.5	0.3659	±400	0.99692	Optical-open loop (air)

V_1 device demonstrates potential for alternative (magnetic-insensitive) sensing applications, including actuators leveraging controlled cooling and heating effects.

Conclusion

In conclusion, this study introduces a high-performance MEMS magnetic sensor based on a smart tunable resonator, offering distinct advantages over existing technologies. The device operates by tuning the resonance frequency of a curved microbeam through the combined effects of axially induced thermal stress and Lorentz force. This force modulates the stiffness of the microstructure, resulting in a measurable shift in resonance frequency. By quantifying this frequency shift, the strength and direction of the applied magnetic field can be accurately determined. The proposed sensor exhibits good linearity across a broad range of magnetic field strengths, significantly enhancing its applicability. A key innovation lies in its smart tunability, achieved through a unique design that incorporates multiple actuation mechanisms. This feature allows for adjustable sensitivity profiles depending on the actuation configuration, offering flexibility to address diverse sensing and actuation requirements. The ability to tailor sensitivity and power consumption distinguishes this sensor from conventional devices in the literature. Furthermore, the sensor operates effectively at atmospheric pressure, eliminating the need for vacuum packaging typically required for high-performance MEMS resonators. This advantage simplifies system integration and reduces manufacturing costs, increasing its accessibility for a wide range of applications. Moreover, overall, this smart tunable MEMS magnetic sensor represents a significant advancement in the development of intelligent sensing technologies, providing a versatile and efficient platform for next-generation applications.

Author contributions
Hanin Amara carried out research, performed simulations, paper drafting and editing. Nadeem Beigh performed formal analysis, graphical representation, paper drafting and editing. Nouha Alcheikh conceived the research, designed the device, performed experiments prepared the measurement setup, supervised the experiments, managed the funding, analysis and paper drafting. All the authors discussed the simulated results, measured results, and prepared the paper.

Conflict of interest
The authors declare no competing interests.

References
1. Liu, J. et al. Piezoelectric thin films and their applications in MEMS: a review. *J. Appl. Phys.* **137**, 2 (2025).
2. Algamili, A. S. et al. A review of actuation and sensing mechanisms in MEMS-based sensor devices. *Nanoscale Res. Lett.* **16**, 16 (2021).
3. Ma, X. et al. MEMS piezo-resistive force sensor based on DC sputtering deposited amorphous carbon films. *Sens. Actuators A Phys.* **303**, 111700 (2020).
4. Mu, Y. et al. An enhanced MEMS-based polyimide capacitive-type relative-humidity sensor with halloysite nanotube as a modifier. *Microchem. J.* **191**, 108934 (2023).
5. Fischer, A. C. et al. Integrating MEMS and ICs. *Microsyst. Nanoeng.* **1**, 15005 (2015).
6. Iqbal, S. & Malik, A. A review on MEMS based micro displacement amplification mechanisms. *Sens. Actuators A Phys.* **300**, 111666 (2019).
7. Gross, S. et al. Dynamic nuclear magnetic resonance field sensing with part-per-trillion resolution. *Nat. Commun.* **7**, 13702 (2016).
8. Ruggeri, J., Ausserlechner, U., Köck, H. & Dowling, K. M. Inverted pyramid 3-axis silicon Hall-effect magnetic sensor with offset cancellation. *Microsyst. Nanoeng.* **11**, 1 (2025).
9. Behera, B., Borole, U. P., Khan, J., Barshilia, H. C. & Chowdhury, P. Fabrication of industrial grade GMR multilayer magnetic sensors for non-recording applications. *Microelectron. Eng.* **298**, 112311 (2025).
10. Valadeiro, J. et al. Hybrid integration of magnetoresistive sensors with MEMS as a strategy to detect ultra-low magnetic fields. *Micromachines (Basel)* **7**, 88 (2016).
11. Keller, P. Magnetic Field Sensing Techniques. in *Magnetic Measurement Techniques for Materials Characterization* 275–299 (Springer International Publishing, Cham,). https://doi.org/10.1007/978-3-030-70443-8_12. (2021).
12. Valle, J. J., Sánchez-Chiva, J. M., Fernández, D. & Madrenas, J. Design, fabrication, characterization and reliability study of CMOS-MEMS Lorentz-force magnetometers. *Microsyst. Nanoeng.* **8**, 103 (2022).
13. Zhou, Z., Zhang, K. & Leng, Q. Tunneling magnetoresistance (TMR) materials and devices for magnetic sensors. in *Spintronics* 51–92 (Wiley, 2022). https://doi.org/10.1002/9781119698968.ch3.

14. Li, M., Sonmezoglu, S. & Horsley, D. A. Extended bandwidth Lorentz force magnetometer based on quadrature frequency modulation. *J. Microelectromech. Syst.* **24**, 333–342 (2015).

15. Du, H., Zhou, G., Zhao, Y., Chen, G. & Chau, F. S. Magnetic field sensor based on coupled photonic crystal nanobeam cavities. *Appl. Phys. Lett.* **110**, 6 (2017).

16. Herrera-May, A. L., López-Huerta, F. & Aguilera-Cortés, L. A. *MEMS Lorentz force magnetometers*. In High Sensitivity Magnetometers, 253–277 (2016).

17. Tu, C., Ou-Yang, X., Wu, Y. & Zhang, X. Single-structure 3-axis Lorentz force magnetometer based on an AlN-on-Si MEMS resonator. *Microsyst. Nanoeng.* **10**, 58 (2024).

18. Zhang, T., Liu, R., Yang, J. & Wang, X. A micro-force measurement system based on Lorentz force particle analyzer for the cleanliness inspection of metal materials. *J. Microelectromech. Syst.* **31**, 143–149 (2022).

19. Park, B., Li, M., Liyanage, S. & Shafai, C. Lorentz force based resonant MEMS magnetic-field sensor with optical readout. *Sens. Actuators A Phys.* **241**, 12–18 (2016).

20. Khan, F. & Younis, M. I. Investigation of on-chip integrated inductors fabricated in SOI-MUMPs for RF MEMS ICs. *Analog Integr. Circuits Signal. Process.* **102**, 585–591 (2020).

21. Zhang, Y. et al. A novel design of a MEMS resonant accelerometer with adjustable sensitivity. *Sens. Actuators A Phys.* **379**, 115859 (2024).

22. Yi, Z. et al. Sensor-actuator integration for intelligent devices. *Device* **3**, 100717 (2025).

23. Li, M. et al. Lorentz force magnetometer using a micromechanical oscillator. *Appl. Phys. Lett.* **103**, 17 (2013).

24. Yaqoob, U., Lenz, W. B., Alcheikh, N., Jaber, N. & Younis, M. I. Highly selective multiple gases detection using a thermal-conductivity-based MEMS resonator and machine learning. *IEEE Sens. J.* **22**, 19858–19866 (2022).

25. Alcheikh, N., Hajjaj, A. Z., Jaber, N. & Younis, M. I. Electrothermally actuated tunable clamped-guided resonant microbeams. *Mech. Syst. Signal. Process.* **98**, 1069–1076 (2018).

26. Alcheikh, N., Kosuru, L., Kazmi, S. N. R. & Younis, M. I. In-plane air damping of micro- and nano- mechanical resonators. *J. Micromech. Microeng.* **30**, 035007 (2020).

27. Alcheikh, N., Ben Mbarek, S. & Younis, M. I. An ultrasensitive low-to-medium vacuum pressure sensor using a resonant microstructure. *IEEE Sens. J.* **24**, 23520–23526 (2024).

28. Alcheikh, N., Mbarek, S. B., Ouakad, H. M. & Younis, M. I. A highly sensitive and wide-range resonant magnetic micro-sensor based on a buckled micro-beam. *Sens. Actuators A Phys.* **328**, 112768 (2021).

29. Sanchez-Chiva, J. M., Valle, J., Fernandez, D. & Madrenas, J. A mixed-signal control system for Lorentz-force resonant MEMS magnetometers. *IEEE Sens. J.* **19**, 7479–7488 (2019).

30. Indianto, M. A., Toda, M. & Ono, T. Comprehensive study of magnetostriction-based MEMS magnetic sensor of a FeGa/PZT cantilever. *Sens. Actuators A Phys.* **331**, 112985 (2021).

31. Kumar, V., Mazrouei Sebdani, S. & Pourkamali, S. Sensitivity enhancement of a Lorentz force MEMS magnetometer with frequency modulated output. *J. Microelectromech. Syst.* **26**, 870–878 (2017).